



# Cellular heterojunctions fabricated through the sulfurization of MOFs onto ZnO for high-efficient photoelectrochemical water oxidation

Jian Zhou, Awu Zhou, Lun Shu, Ming-Cheng Liu, Yibo Dou\*, Jian-Rong Li\*

Beijing Key Laboratory for Green Catalysis and Separation and Department of Chemistry and Chemical Engineering, College of Environmental and Energy Engineering, Beijing University of Technology, Beijing 100124, PR China



## ARTICLE INFO

### Keywords:

Photoelectrochemical water oxidation  
ZnO-based heterojunction  
Sulfurization of MOFs  
Cellular structure  
Co-catalyst

## ABSTRACT

Photoelectrochemical (PEC) water splitting offers a promising way for producing clean and renewable hydrogen fuel, but how to improve the solar conversion efficiency is still a challenge. Herein, the sulfurization of metal-organic frameworks (MOFs) onto the semiconductor ZnO to fabricate heterojunctions for PEC water oxidation was proposed. Cellular ZnO@ZnS, ZnO@CoS, and ZnO@ZnS/CoS heterostructured catalysts thus obtained through the direct sulfurization of ZnO@zeolitic-imidazolate-frameworks (ZnO@ZIFs) composites exhibit excellent PEC performances. Particularly, the ZnO@ZnS/CoS represents a largely improved photoconversion efficiency (0.65% at 0.14 V) and photocurrent density ( $2.46 \text{ mA cm}^{-2}$  at 0.6 V) under full spectrum illumination, outperforming those of previously reported ZnO-based catalysts in neutral medium. Clearly, their special cellular structure affords rich exposed active sites and long incident photon transport pathway for well light absorption. And, the suitable band matching with strong electronic coupling in the integrated heterojunctions facilitates the effective electron-hole separation. Furthermore, CoS acting as co-catalyst can speed up the hole transfer and simultaneously participate in the surface water oxidation, which leads to the lower oxygen evolution barrier for ZnO@CoS and ZnO@ZnS/CoS. This MOF-derivative decoration approach could be expanded to fabricate other composite photoanodes for a variety of energy storage and conversion applications.

## 1. Introduction

Photoelectrochemical (PEC) water splitting has been considered as one of the appealing strategies to obtain highly-efficient and eco-friendly hydrogen energy, by integrating solar energy collection and water electrolysis into a single photoelectrode [1–3]. Accordingly, a number of semiconductor materials have been explored as photoanodes (e.g. TiO<sub>2</sub>,  $\alpha$ -Fe<sub>2</sub>O<sub>3</sub>, BiVO<sub>4</sub>, and ZnO) for PEC water splitting due to their positive electron mobility, low cost-efficiency, and good environmental compatibility [4–7]. Despite of well performances, the drawbacks of utilizing these semiconductors with unsatisfied electron-hole separation rates and slow interfacial kinetics always induce electron-holes recombination and/or anodic corrosion, rebating their PEC water oxidation performance [7,8]. As a result, great amounts of efforts have been devoted to improve the overall PEC performance of photoanode, including fabricating heterojunctions (e.g. GaN/ZnO and ZnO/CdTe) [9,10], constructing hierarchical structures (e.g. hollow urchin-like  $\gamma$ -TaON, sandwich structured CdS-Au-TiO<sub>2</sub>) [11,12], applying noble metal sensitization (e.g. Au/TiO<sub>2</sub> and Au@Pd/UiO-66(Zr<sub>85</sub>Ti<sub>15</sub>)) [13,14], and/or integrating co-catalysts (e.g. IrO<sub>2</sub> and Co-Pt) [15,16].

Nevertheless, developing new materials or methodologies to fabricate photoanodes with high energy conversion efficiency and desirable stability for PEC water splitting still remain a challenge.

In order to enhance the PEC water oxidation activity, as mentioned above, an effective strategy is to deliberately design hierarchically structured heterojunctions by the introduction of oxygen evolution catalyst (OEC) with semiconductor. Resulting composite photoanodes can thus afford prolonged light-traveling length for efficient solar light utilization, suitable energy band structure for fast carrier transfer, and lower oxygen evolution barrier to drive the water oxidation [17–19]. Recently, metal-organic frameworks (MOFs) and their derivatives/composites (e.g. NiCo-MOF nanosheets, NH<sub>2</sub>-MIL-101(Cr), and CoS<sub>1.097</sub>/nitrogen-doped carbon nanosheets) [20–22], have been attracting intense research interest for the electrocatalytic or photocatalytic water splitting because their inherited/generated large surface areas and tunable pore structures are quite favorable for enhancing catalytic activity [23–25]. Despite these endeavors, their use as photoanode catalysts for the PEC water splitting has been rarely reported, probably due to their poor light capture capability and/or sluggish reaction kinetics.

\* Corresponding author.

E-mail addresses: [douyb@bjut.edu.cn](mailto:douyb@bjut.edu.cn) (Y. Dou), [jrli@bjut.edu.cn](mailto:jrli@bjut.edu.cn) (J.-R. Li).

Based on above considerations, we propose that the integration of semiconductor with MOF derivatives into a sophisticated structure as the photoanode might achieve enhanced PEC water oxidation, which would have the following advantages: (i) The outward shell of MOF derivatives with high surface area and rich porosity inherited from themselves can endow long optical paths for efficient light absorption and abundant exposed active sites for fast electron-holes generation and electrochemical reaction; (ii) Suitable band matching can be achieved feasibly by tuning the types of metal centers in the MOF, thereby facilitating the fabrication of the heterojunction and avoiding undesired recombination of volume charges correspondingly; (iii) Transition metal-based MOFs are ideal candidates as the templates for the construction of the OEC (e.g. CoS, Co<sub>3</sub>O<sub>4</sub>, and NiP) with high surface areas and hierarchically porous structures [23,25], which employed as co-catalysts can facilitate the electron/hole transfer and then be in favor of fast water oxidation.

Herein, we designed and fabricated ZnO@ZnS, ZnO@CoS, and ZnO@ZnS/CoS heterojunctions with cellular structure by the *in situ* growth of zeolitic-imidazolate-frameworks (ZIFs), ZnCo-ZIF, ZIF-8 and –67 on semiconductor ZnO nanorods and the subsequent treatment of sulfurization (Fig. 1a). These heterojunction composites, being directly employed as photoanodes exhibit largely enhanced PEC water oxidation performance due to the strong light-harvesting capability, efficient electron-hole separation, and fast surface water oxidation generated from special cellular morphology, suitable band matching structure. Remarkably, co-catalyst CoS as OEC facilitates the acceleration of the electron/holes transfer at the interface of photoanode/electrolyte and

thus promotes the surface water oxidation kinetics. Meanwhile, CoS combined with ZnS and ZnO can form a ternary heterojunction, in which CoS acting a hole-trapping site can suppress the recombination of photogenerated electron-hole pairs and thus boost the PEC water oxidation performance. Consequently, the ZnO@ZnS/CoS gave rise to a largely enhanced photocurrent density (2.46 mA cm<sup>–2</sup> at 0.6 V), low onset potential (–0.35 V), and improved photoconversion efficiency (0.65% at 0.14 V) with high stability under full spectrum illumination, much superior to those of previously reported ZnO-based photoanodes in neutral medium.

## 2. Experimental

### 2.1. Preparation of ZnO arrays

ZnO arrays on indium tin oxide (ITO) glass substrate were synthesized according to a previously reported method [10]. Typically, the zinc acetate (0.132 g) was dissolved in dehydrated ethanol (100 mL) under ultrasonic agitation. The above solution was spin-coated onto the pre-treated ITO substrate and subsequently annealed at 350 °C in air for 30 min to form a layer of ZnO seeds. The substrate was then immersed into a 60 mL reaction solution containing Zn(NO<sub>3</sub>)<sub>2</sub>·6H<sub>2</sub>O (60 mM) and hexamethylenetetramine (HMT, 60 mM), and then this system was transferred into a Teflon-lined autoclave and heated at 110 °C for 24 h. Finally, the resulting ZnO arrays were washed repeatedly with distilled water and dried in air.

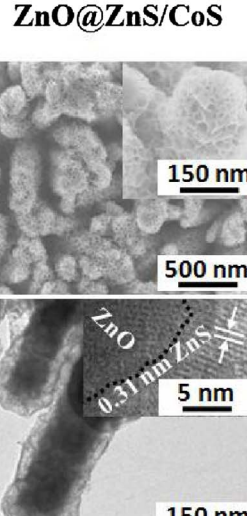
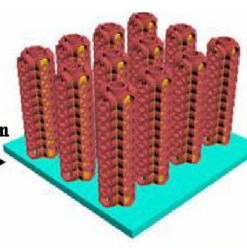
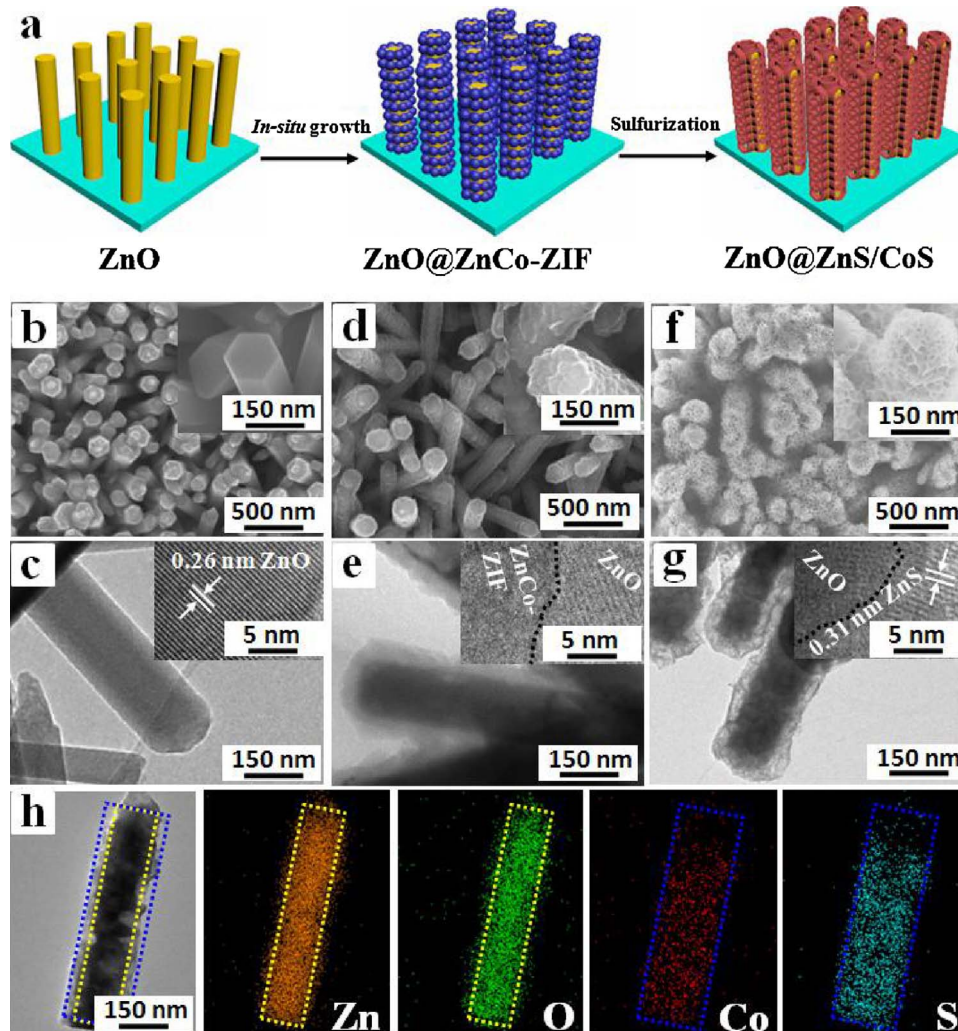


Fig. 1. (a) Schematic illustration for the fabrication of cellular ZnO@ZnS/CoS. (b and c) SEM and TEM images of ZnO, (d and e) SEM and TEM images of ZnO@ZnCo-ZIF, (f and g) SEM and TEM images of ZnO@ZnS/CoS, respectively. (h) TEM with corresponding EDX mapping images of ZnO@ZnS/CoS.



## 2.2. Preparation of $\text{ZnO}@\text{ZnCo-ZIF}$ , $\text{ZnO}@\text{ZIF-8}$ , and $\text{ZnO}@\text{ZIF-67}$ arrays

$\text{ZnO}@\text{ZnCo-ZIF}$  arrays were prepared via a facile hydrothermal method [26,27]. Typically, 2-methylimidazole (0.1 mg) and  $\text{Co}(\text{NO}_3)_2 \cdot 6\text{H}_2\text{O}$  (0.01 mg) were dissolved into a mixed solvent of DMF and  $\text{H}_2\text{O}$  (16 mL, v:v = 4:1). Above prepared  $\text{ZnO}$  arrays were then immersed into the solution, and this system was transferred into a Teflon-lined autoclave and heated at 70 °C for 2 h. After cooling down the temperature, the prepared  $\text{ZnO}@\text{ZnCo-ZIF}$  arrays were washed repeatedly with DMF and ethanol and dried in vacuum at 60 °C for 12 h.  $\text{ZnO}@\text{ZIF-8}$  arrays were prepared by a similar procedure to that of  $\text{ZnO}@\text{ZnCo-ZIF}$ . 2-Methylimidazole (0.1 mg) was dissolved into a mixed solvent of DMF and  $\text{H}_2\text{O}$  (16 mL, v:v = 1:1). The above prepared  $\text{ZnO}$  arrays were then immersed into the mixed solvent, and the system was transferred into a Teflon-lined autoclave and heated at 70 °C for 2 h. After cooling down the temperature, the resulting  $\text{ZnO}@\text{ZIF-8}$  arrays were washed repeatedly with DMF and ethanol, and dried in vacuum at 60 °C for 12 h. As for  $\text{ZnO}@\text{ZIF-67}$ , 2-Methylimidazole (0.1 mg) and  $\text{Co}(\text{NO}_3)_2 \cdot 6\text{H}_2\text{O}$  (0.01 mg) were in sequence dissolved into the solvent of DMF (16 mL). The above prepared  $\text{ZnO}$  arrays were then immersed into the mixed solvent, and the reaction system was transferred into a Teflon-lined autoclave and heated at 70 °C for 2 h. After cooling down the temperature, the resulted  $\text{ZnO}@\text{ZIF-67}$  arrays were washed repeatedly with DMF and ethanol, and dried in vacuum at 60 °C for 12 h.

## 2.3. Preparation of $\text{ZnO}@\text{ZnS/CoS}$ , $\text{ZnO}@\text{ZnS}$ , and $\text{ZnO}@\text{CoS}$ arrays

The  $\text{ZnO}@\text{ZnS/CoS}$  arrays were prepared via the sulfurization of the  $\text{ZnO}@\text{ZnCo-ZIF}$ . The thioacetamide (0.05 g) was firstly dissolved in 20 mL ethanol, followed by immersing the  $\text{ZnO}@\text{ZnCo-ZIF}$  into the solution for 0.5–4 h at 70 °C. The obtained  $\text{ZnO}@\text{ZnS/CoS}$  was washed by ethanol and water, and then dried in vacuum at 60 °C for 2 h. Similarly,  $\text{ZnO}@\text{ZnS}$  and  $\text{ZnO}@\text{CoS}$  arrays were obtained via the sulfurization of the  $\text{ZnO}@\text{ZIF-8}$  and  $\text{ZnO}@\text{ZIF-67}$  arrays, respectively.

## 2.4. Preparation of $\text{ZnS}$ , $\text{CoS}$ , $\text{ZnS/CoS}$ , $\text{ZnO}@\text{ZnS}$ , $\text{ZnO}@\text{CoS}$ , and $\text{ZnO}@\text{ZnS/CoS}$ powders

Firstly, the templates that ZIF-8, ZIF-67, ZnCo-ZIF,  $\text{ZnO}@\text{ZIF-8}$ ,  $\text{ZnO}@\text{ZIF-67}$  and  $\text{ZnO}@\text{ZnCo-ZIF}$  powders were synthesized according to modified reported method [28,29]. Then, the  $\text{ZnS}$  was prepared by the sulfurization of ZIF-8. Briefly, thioacetamide (0.187 g) was dissolved in 40 mL ethanol, in which ZIF-8 powder (50 mg) was added. Resulting solution was refluxed for 1 h under stirring. The obtained  $\text{ZnS}$  was collected via centrifugation, washed thoroughly with anhydrous ethanol and dried in vacuum at 60 °C for 12 h. Meanwhile, the  $\text{CoS}$ ,  $\text{ZnS/CoS}$ ,  $\text{ZnO}@\text{ZnS}$ ,  $\text{ZnO}@\text{CoS}$ , and  $\text{ZnO}@\text{ZnS/CoS}$  were synthesized by a similar procedure, by using ZIF-67, ZnCo-ZIF,  $\text{ZnO}@\text{ZIF-8}$ ,  $\text{ZnO}@\text{ZIF-67}$ , and  $\text{ZnO}@\text{ZnCo-ZIF}$  powders as the precursors, respectively. For powdered  $\text{ZnO}@\text{ZnS/CoS}$  photoanode,  $\text{ZnO}@\text{ZnS/CoS}$  powders (2 mg) were added into the mixture solution ( $\text{H}_2\text{O}:\text{PrOH}:\text{Nafion} = 650:250:100 \mu\text{L}$ ), and sonicated for ~30 min. The suspension (20  $\mu\text{L}$ ) was spin-coated onto the ITO glass slide (1 cm × 2 cm), and dried at room temperature to obtain the powdered  $\text{ZnO}@\text{ZnS/CoS}$  photoanode [30].

## 2.5. Characterization

Powder X-ray diffraction (PXRD) was investigated in a Rigaku XRD-6000 diffractometer with  $\text{Cu K}\alpha$  radiation ( $\lambda = 0.1542 \text{ nm}$ ) at 40 kV and 30 mA. X-ray photoelectron spectroscopy (XPS) measurements were carried out using an ESCALAB 250 instrument. The surface area and pore distribution of  $\text{ZnO}$ ,  $\text{ZnO}@\text{ZnS}$ ,  $\text{ZnO}@\text{CoS}$ , and  $\text{ZnO}@\text{ZnS/CoS}$  samples were measured on a Micrometrics surface area analyzer (ASAP 2020). Fourier transform infrared (FT-IR) spectra were recorded

using a Vector 22 (Bruker) spectrophotometer with a resolution of  $2 \text{ cm}^{-1}$ . Solid-state UV-vis diffuse reflectance spectra were measured on a UV-2600 spectrophotometer in the range of 200 ~ 800 nm. Photoluminescence (PL) emission spectra were recorded on an F-4600 FL spectrophotometer equipped with a xenon lamp and quartz carrier at room temperature and time-resolved PL spectra were recorded on an Edinburgh Instruments FL 900 fluorimeter. Scanning electron microscope (SEM) image combined with energy dispersive X-ray (EDX) spectroscopy was performed on Zeiss SUPRA 55 with an accelerating voltage of 20 kV. Transmission electron microscopy (TEM) image and EDX mapping were observed by a JEOL JEM-2100 and a JEM-2100F of an accelerating voltage of 200 kV, respectively.

## 2.6. Electrochemical measurements

All PEC tests were operated on a electrochemistry workstation (Zennium Pro) in a three-electrode mode with a photoanode as the working electrode, a Pt plate as the counter electrode, a saturated calomel electrode (SCE) as the reference electrode, and 0.5 M  $\text{Na}_2\text{SO}_4$  (pH = 6.8) solution as electrolyte medium. Highly-arrayed  $\text{ZnO}$ ,  $\text{ZnO}@\text{ZnS}$ ,  $\text{ZnO}@\text{CoS}$ , and  $\text{ZnO}@\text{ZnS/CoS}$  films were directly employed as a photoanode with an area of  $1 \text{ cm} \times 2 \text{ cm}$ . For comparison, the  $\text{ZnO}@\text{MOF}$ -derived powders based photoanodes were prepared using a spin-coating method onto the ITO substrate glass. All water oxidation photoelectrodes were illuminated under xenon lamp (PLS-SXE300) with an irradiance intensity of  $100 \text{ mW cm}^{-2}$ . And the visible light illumination was obtained through a 420 nm long-wave pass filter. The photocurrent was measured by current-voltage ( $J$ - $V$ ) curve at a scan rate of  $10 \text{ mV s}^{-1}$ . The electrochemical impedance spectroscopy (EIS) was recorded under the dark and light ( $100 \text{ mW cm}^{-2}$ ) condition in 0.5 M  $\text{Na}_2\text{SO}_4$  solution over a frequency range from  $10^5$  to  $10^{-1} \text{ Hz}$ .

## 3. Results and discussion

Since three  $\text{ZnO}@\text{ZIF}$ -derivatives have similar fabrication procedures, morphologies, and structures, the fabrication and characterizations of  $\text{ZnO}@\text{ZnS/CoS}$  were described in detail herein. Quasi-vertically aligned  $\text{ZnO}$  nanorods with an average length of  $\sim 3.2 \mu\text{m}$  were firstly prepared, as confirmed by the SEM image (Figs. 1b and S1). The TEM image reveals that the diameter of  $\text{ZnO}$  nanorods is  $\sim 150 \text{ nm}$ , and the high-resolution TEM (HR-TEM) shows the lattice spacing is  $\sim 0.26 \text{ nm}$ , which can be ascribed to the (002) plane of  $\text{ZnO}$  (Fig. 1c) [29]. After the *in situ* growth of ZnCo-ZIF onto the  $\text{ZnO}$  surface, the color of the film changed from white to light purple (Fig. S2), supposedly through a self-sacrificial template process [28,29]. The SEM image shows that the  $\text{ZnO}@\text{ZnCo-ZIF}$  arrays still kept well-defined structure but the surface was covered with ZnCo-ZIF particles (Fig. 1d). And, a core-shell structure was successfully obtained as observed from the TEM image (Figs. 1e and S3). Clearly, ZnCo-ZIF nanoparticles with an average diameter of  $\sim 20 \text{ nm}$  were tightly attached to the surface of  $\text{ZnO}$ . It should be pointed out that the thickness of the ZnCo-ZIF shell can be adjusted from  $\sim 20$  to  $\sim 80 \text{ nm}$  by controlling solvothermal growth time from 1 to 4 h, as demonstrated by powder X-ray diffraction (PXRD) (Fig. S4).

After sulfurization treatment, the  $\text{ZnO}@\text{ZnCo-ZIF}$  was gradually etched into hierarchically structured  $\text{ZnO}@\text{ZnS/CoS}$  along with the color changes from light purple to gray (Figs. 1f and S2), in which the cellular  $\text{ZnO}@\text{ZnS/CoS}$  nanorods with the uniform structured  $\text{ZnS/CoS}$  shell were observed from the cross-sectional SEM image (Fig. S5) and TEM image (Fig. 1g). Simultaneously, HR-TEM image of the edge section confirms the interplanar distance to be  $\sim 0.26$  and  $\sim 0.31 \text{ nm}$ , being ascribed to the (002) plane of  $\text{ZnO}$  and the (100) plane of  $\text{ZnS}$ , respectively [31]. But, no obvious interplanar region for  $\text{CoS}$  was observed because of its amorphous structure [32]. Furthermore, the corresponding energy dispersive X-ray (EDX) mapping analysis illustrates the homogeneous distribution of elements in  $\text{ZnO}@\text{ZnS/CoS}$  (Fig. 1h). It was found that Zn and O elements are mainly located in the core part

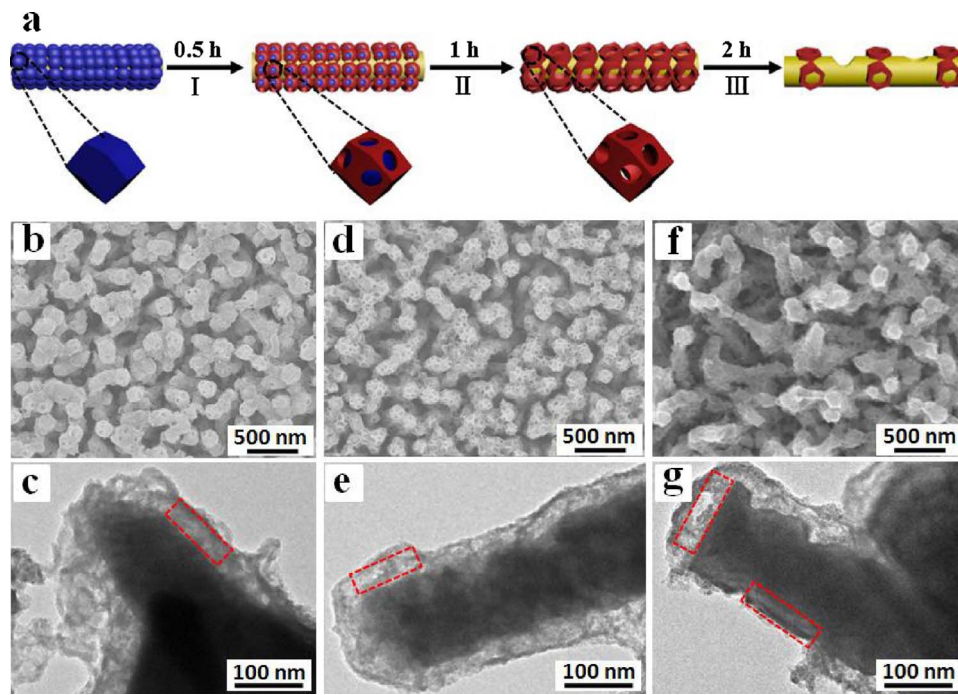


Fig. 2. (a) Schematic illustration of the formation process of the hierarchically structured ZnO@ZnS/CoS. SEM and TEM images as the function of sulfurization time of 0.5 (b and c), 1 h (d and e), and 2 h (f and g), respectively.

of the nanorods, while Co and S elements are homogeneously distributed throughout the shell, implying most of the ZnS located between ZnO and CoS. Meanwhile, the EDX spectrum and corresponding elemental composition reveal that the weight ratio of Co and S are  $\sim 3.4$ , and  $\sim 7.3\%$ , respectively, being relatively lower than those of Zn ( $\sim 69.0\%$ ) and O ( $20.3\%$ ) (Fig. S6). Furthermore, the diameter of core ZnO in ZnO@ZnS/CoS decreased to  $\sim 135$  nm, compared with that in ZnO@ZnCo-ZIF with the diameter of  $\sim 145$  nm, illustrating ZnO nanorods were partially transformed into ZnS, after the sulfurization treatment. Similarly, ZnO@ZnS and ZnO@CoS with well-defined cellular structures were fabricated through firstly the *in situ* growth of ZIF-8 or ZIF-67 onto the ZnO nanorods to form ZnO@ZIF-8 and ZnO@ZIF-67, and then sulfurization, respectively (Fig. S7).

The formation mechanism of the cellular ZnO@ZnS/CoS obtained by the self-sacrificial ZnCo-ZIF template was further investigated, which is schematically illustrated through proposed three steps showed in Fig. 2a. At step I, sulfide ions ( $S^{2-}$ ) provided by the hydrolysis of thioacetamide react with metal ions released from the ZnCo-ZIF shell of ZnO@ZnCo-ZIF to generate a thin layer of ZnS/CoS externally, while the inner part is still consist of ZnCo-ZIF. With prolonging the reaction time (step II), the reaction of outer diffused  $S^{2-}$  ions with inner metal ions results in the exhaustion of ZnCo-ZIF and simultaneously the formation of cellular ZnS/CoS on the surface of ZnO. Further prolonging the reaction time, the  $S^{2-}$  ions react with the metal sources from the surface of ZnO core, leading to the weak adhesion between inner ZnO and outer metal sulfides, thereby resulting in collapse of cellular structure (step III).

This speculation was then confirmed by the process of the morphology evolution and the crystallization variation as the function of the sulfurization time, *via* SEM, TEM, and PXRD characterizations. Comparing with that of pristine ZnO@ZnCo-ZIF (Fig. 1d), the edge of ZnCo-ZIF was partially etched into ZnS/CoS when the sulfurization treatment reached to 0.5 h (Fig. 2b). The etching process took precedence over the edge between the skeleton and the rest part [33], leading to the contraction of the middle plane surface and the formation of the gap between the ZnS/CoS shell and ZnCo-ZIF core (Fig. 2c). The PXRD reveals that the diffraction peaks came from ZnCo-ZIF diminished or even vanished when comparing with those of pristine ZnO@ZnCo-ZIF (Fig. S8). Interestingly, further prolonging the sulfurization time to

1 h, hierarchically structured ZnO@ZnS/CoS with large cellular pores was formed and the increasing roughness of the surface was clearly observed (Fig. 2d and e). Meanwhile, the PXRD patterns of ZnCo-ZIF disappeared completely, being accompanied with the appearance of ZnS diffraction (Fig. S8). Further prolonging time to 2 h, the  $S^{2-}$  could diffuse into the inner core and react with  $Zn^{2+}$  supplied by ZnO, resulting in the formation of more ZnS. The excessive sulfurization could lead to collapse of cellular structure (Fig. 2f and g) and the destruction of interfacial interaction between ZnO and cellular ZnS/CoS to some degree, which are unfavorable for the PEC water oxidation. This will be discussed in below. In addition, the whole variation process was also further confirmed by the directly sulfurization of pristine ZnCo-ZIF powder (Fig. S9).

The detailed composition and structural characterizations of these obtained ZnO, ZnO@ZnCo-ZIF, and ZnO@ZnS/CoS arrays were further investigated. As shown in Fig. 3a, comparing with wurtzite-structured ZnO, the (011), (002), and (112) lattice planes of ZnCo-ZIF after the decoration onto the surface of ZnO was observed, illustrating the formation of the composite ZnO@ZnCo-ZIF. The FT-IR spectra also illustrate the existence of ZnCo-ZIF shell onto the ZnO (Fig. S10), in which the band at  $421\text{ cm}^{-1}$  and the region of  $1350\text{--}1500\text{ cm}^{-1}$  were assigned to the Zn–N stretch mode and the imidazole ring stretch vibration, respectively [34]. After the sulfurization treatment, a weak broad diffraction at  $28.5^\circ$  from ZnS was observed in ZnO@ZnS/CoS. And, no obvious diffraction peak of CoS was observed in it, being consistent with the HR-TEM result (Fig. 1g).

Meanwhile, X-ray photoelectron spectroscopy (XPS) was used to better characterize and understand the heterostructured feature of ZnO@ZnS/CoS. The XPS survey spectra show that no obvious impurities present in ZnO@ZnCo-ZIF and ZnO@ZnS/CoS (Fig. S11a). From the high-resolution scans of Zn 2p, the binding energies of Zn  $2p_{1/2}$  and Zn  $2p_{3/2}$  were evaluated to be at 1021.59 and 1044.54 eV for pristine ZnO nanorods [18]. After growing ZnCo-ZIF onto the ZnO, both the Zn  $2p_{1/2}$  and Zn  $2p_{3/2}$  peaks shifted to 1021.83 and 1044.91 eV, respectively, indicating the existence of interactions between ZnO and ZnCo-ZIF (Fig. 3b). Obviously, the shifts of Zn 2p peaks could be attributed to the reaction of Zn resource supplied by ZnO surface with 2-methylimidazole ligand. Most importantly, the binding energies migrated to higher energy levels at 1022.93 and 1045.96 eV after the

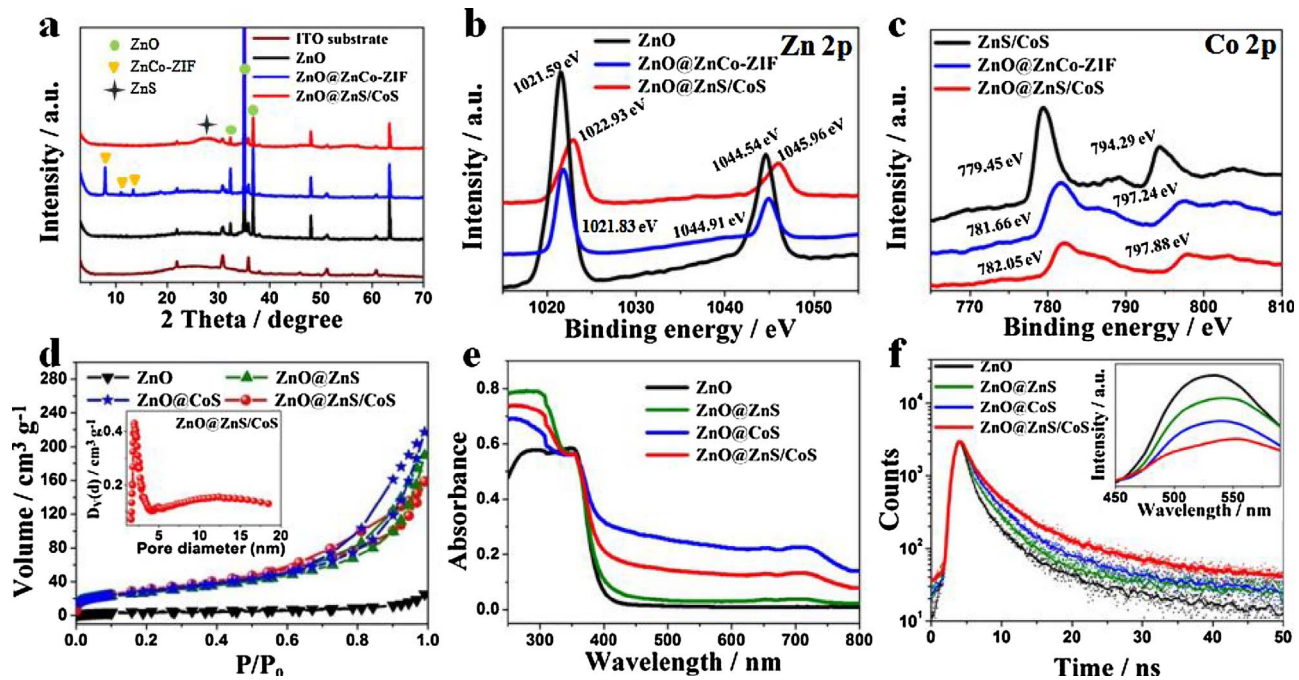


Fig. 3. (a) PXRD patterns of the indium tin oxide (ITO) substrate, ZnO, ZnO@ZnCo-ZIF, and ZnO@ZnS/CoS on the substrate. (b) Zn 2p XPS spectra of ZnO, ZnO@ZnCo-ZIF, and ZnO@ZnS/CoS. (c) Co 2p XPS spectra of ZnS/CoS, ZnO@ZnCo-ZIF, and ZnO@ZnS/CoS. (d)  $N_2$ -adsorption/desorption isotherms (inset: pore size distribution), (e) UV-vis diffuse reflectance, and (f) time-resolved PL spectra (inset: PL spectra) of ZnO, ZnO@ZnS, ZnO@CoS, and ZnO@ZnS/CoS, respectively.

sulfurization treatment, indicating the existence of electron coupling interaction between ZnO and ZnS. In addition, the binding energies of Co  $2p_{3/2}$  and Co  $2p_{1/2}$  with main peaks at 782.05 and 797.88 eV for ZnO@ZnS/CoS also exhibited a positive shift compared to that of ZnO@ZnCo-ZIF. And, the binding energy of Co  $2p_{3/2}$  for the ZIF-derived bulk ZnS/CoS composite increased from 779.45 to 782.05 eV. These results reveal the occurrence of self-oxidation of Co<sup>II</sup> to Co<sup>III</sup>, which is in favor of rapid electron/holes transfer on the interface of photoanode/electrolyte and acceleration of surface water oxidation kinetics (Fig. 3c) [35]. Simultaneously, the binding energy shifts for S  $2p_{3/2}$  and S  $2p_{1/2}$  were also observed in ZnO@ZnS/CoS by comparing with those of bulk ZnS/CoS, further confirming interaction between ZnO and ZnS/CoS (Fig. S11b).

In addition,  $N_2$  adsorption/desorption measurements were carried out to investigate the surface area and pore-size distribution of these composites. As shown in Fig. 3d, all three ZnO@MOF-derivatives represent IV-type isotherms with H3-type hysteresis loops ( $P/P_0 > 0.4$ ). Owning to the inheritance of skeleton structure from the MOFs, the surface areas of ZnO@ZnS, ZnO@CoS, and ZnO@ZnS/CoS are 197.3, 195.4, and  $191.8 \text{ m}^2 \text{ g}^{-1}$ , respectively, much larger than that ( $15.1 \text{ m}^2 \text{ g}^{-1}$ ) of bare ZnO powder. The evaluated pore-size distributions are mainly located among 2–5 nm (Fig. 3d, inset), further confirming the hierarchically micro- and meso-porous structure of these composites.

UV-vis diffuse reflectance and photoluminescence (PL) emission combined with time-resolved PL spectra were then utilized to evaluate the light-harvesting capability of these heterojunctions. The pristine ZnO gave an absorption in the UV light region with a band gap of  $\sim 3.18 \text{ eV}$  (Figs. 3e and S12). As for ZnO@ZnS, a stronger UV absorption band with red shift ( $\sim 3.48 \text{ eV}$  band gap) relative to that of ZnO were observed because of the enhanced light absorption of ZIF-8-derived ZnS (Fig. S13) [29]. Interestingly, the visible light responsive CoS affords ZnO@ZnS/CoS and ZnO@CoS with obvious absorption in the visible light region (Figs. 3e and S13), which is favorable for the solar light harvesting. On the other hand, the PL spectra provide hints for the recombination property of photoexcited charge carriers in these materials (Fig. 3f). It was found that the decreased PL intensities follow a

sequence of ZnO < ZnO@ZnS < ZnO@CoS < ZnO@ZnS/CoS, suggesting that the integration of ZnO and ZnS/CoS could suppress the recombination of photogenerated charge carriers. Furthermore, time-resolved PL spectra also measured the lifetimes of electrons in the excited state for all samples by using 325 nm excitation (Fig. 3f). The fluorescence lifetime values were determined to be 3.03, 4.90, 6.42, and 7.06 ns for ZnO, ZnO@ZnS, ZnO@CoS, and ZnO@ZnS/CoS, respectively (Table S1). The prolonged fluorescence lifetimes of ZnO@MOF-derivatives are related to longer-lived electrons, which is in favor of the charge transfer and surface reaction [36], compared with bare ZnO.

PEC water oxidation measurements under full spectrum illumination were finally carried out over ZnO, ZnO@ZnS, ZnO@CoS, and ZnO@ZnS/CoS directly acting as photoanodes. As shown in Fig. 4a, the photocurrent densities of the ZnO@ZIF-derivatives increase significantly in the potential window range of  $-0.6$  to  $0.8 \text{ V}$  vs. saturated calomel electrode (SCE), compared with that of bare ZnO. Particularly, the ZnO@ZnS/CoS exhibits a sharp negative shift of the onset potential from  $-0.20$  to  $-0.35 \text{ V}$  and the maximum photocurrent density of  $2.46 \text{ mA cm}^{-2}$  at  $0.6 \text{ V}$ , which is 1.4, 2.2, and 5.1 times larger than those of ZnO@CoS, ZnO@ZnS, and ZnO, respectively. In addition, the ZnO@ZIF-derivatives that ZnO@ZnS, ZnO@CoS, and ZnO@ZnS/CoS with the special heterostructure exhibit enhanced catalytic activity, which are much higher than their corresponding precursors that ZnO@ZIF-8, ZnO@ZIF-67, and ZnO@ZnCo-ZIF, respectively (Fig. S14). These PEC performances are clearly superior to those of previously reported ZnO-based materials in neutral medium (Table S2). Meanwhile, the ZnO@ZnS, ZnO@ZnS, and ZnO@ZnS/CoS powders formed photoanodes show weaker photocurrent densities because of the lower electron mobility and blockage of active sites (Fig. S15). On the contrary, the unique cellular structure imparts the ZnO@ZnS/CoS photoanode with efficient light harvesting and rich exposed active sites. Moreover, the co-catalyst CoS as holes acceptor facilitates fast holes transportation and water oxidation reaction directly on the surface of ZnO@ZnS, meanwhile the electrons are rapidly channeled via ZnO rods to the counter electrode for effectively suppressing electron-hole recombination, thus accounting for obvious negative shift of the onset

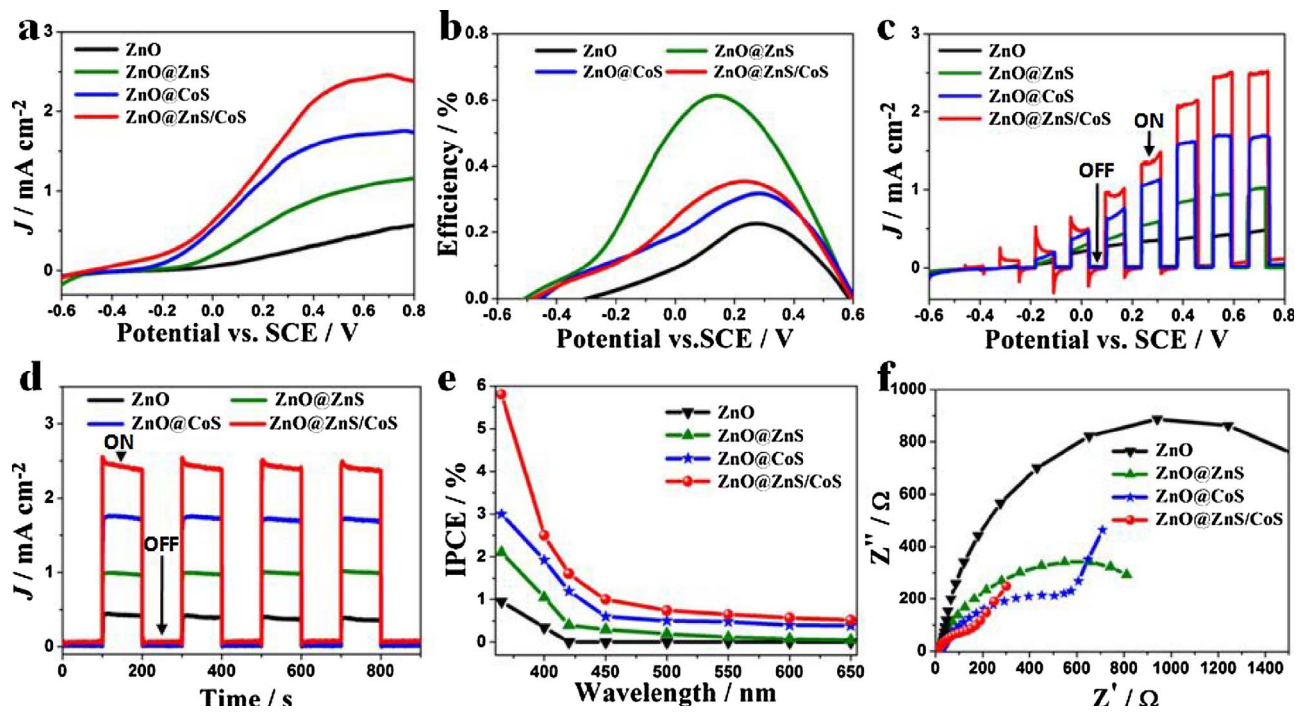


Fig. 4. (a)  $J$ - $V$  curves, (b) photoconversion efficiency as a function of applied voltage, (c)  $J$ - $V$  curves and (d) amperometric current-time ( $I$ - $t$ ) curves at a potential of 0.6 V (vs. SCE) under chopped light illumination, (e) IPCEs measured at an applied voltage of 0.6 V, and (f) EIS measured under full spectrum illumination for ZnO, ZnO@ZnS, ZnO@CoS, and ZnO@ZnS/CoS.

potential and improved current density. In addition, it is found that the PEC activity of photoanodes was related with the sulfurization time (Fig. S16). The ZnO@ZnS/CoS upon 1 h sulfurization treatment with well-defined cellular structure could afford rich active sites and hierarchically porous structure for well light absorption. Correspondingly, ZnO@ZnS/CoS upon 1 h sulfurization treatment possesses the highest current density of  $2.46 \text{ mA cm}^{-2}$  at the potential of 0.6 V, compared with 1.15, 1.91, and  $1.36 \text{ mA cm}^{-2}$  based on the sulfurization time of 0.5, 2, and 4 h, respectively. The effect of ratio for ZnS to CoS on the PEC activity of the ZnO@ZnS/CoS was also investigated by adjusting the concentration of  $\text{Co}^{2+}$  species (Fig. S17). It is found that ZnO@ZnS/CoS exhibits a slightly increased current density with increasing ratio of CoS to ZnS from 1.1:3.4 to 1.0:2.1. The reason is that visible light responsive CoS acting as OEC and holes acceptor can lower energy barrier of water oxidation and facilitate electron transfer. However, a decreased current density was observed by further increasing the ratio from 1.0:2.1 to 2.1:1.0, implying more decoration of CoS would probably affect the light harvesting and carriers transfer for inner ZnS and ZnO, thus rebating the promotion of the PEC activity.

Moreover, it was found that the ZnO@ZnS/CoS photoanode has the maximum photoconversion efficiency ( $\eta$ ) of 0.65% at 0.14 V, higher than those of ZnO@CoS (0.38% at 0.24 V), ZnO@ZnS (0.33% at 0.27 V), and ZnO (0.23% at 0.27 V) (Fig. 4b). The electrochemical impedance spectroscopy (EIS) study also shows that ZnO@ZnS/CoS has the smallest electron transfer resistance, illustrating fastest charge migration in it (Fig. 4f). The observed higher photocurrent density and photoconversion efficiency of the hierarchically structured ZnO@ZnS/CoS could be attributed to three major aspects. Firstly, the MOF-derived cellular porous structures afford prolonged optical paths for the light absorption and high electrochemically active surface area (ECSA) for the exposure of catalytically active sites of the photoanode (Figs. S18–S20). Secondly, an extraordinarily ternary heterojunction formed by ZnO and ZnS/CoS could improve the light-harvesting capability and thus promote the rapid generation of electron-hole pairs by absorbed photons. Thirdly, the derived co-catalyst CoS as an effective OEC and holes acceptor endows the lower oxygen evolution barrier for driving fast surface water oxidation and simultaneously suppresses the

recombination of photogenerated charge carriers. All these factors thus contribute to excellent PEC water oxidation performances of cellular ZnO@MOF-derivatives.

The photoresponsive behaviors of ZnO, ZnO@ZnS, ZnO@CoS, and ZnO@ZnS/CoS were investigated by transient photocurrent measurements (Fig. 4c) and chronoamperometry (Fig. 4d) under chopped light illumination. A steady and prompt photocurrent response was observed for all materials during the ON and OFF cycle of illumination (Fig. 4d). The trend of current densities under illumination is ZnO < ZnO@ZnS < ZnO@CoS < ZnO@ZnS/CoS, being consistent with  $J$ - $V$  curve results (Fig. 4a). Moreover, the incident-photon-to-current conversion efficiency (IPCE) was further investigated (Fig. 4e). It was confirmed that cellular ZnO@ZIF-derivatives have higher PEC activities relative to that of bare ZnO in the region between 365 and 650 nm. Particularly, the ZnO@ZnS/CoS represented a maximum IPCE of 5.92% at 365 nm, compared with ZnO@CoS (2.99%), ZnO@ZnS (2.03%), and ZnO (1.02%). The higher charge injection and separation efficiency illustrates that the MOF-derivative decoration on ZnO allows the resulting photoanode with suppressed recombination of the photogenerated electron-hole pairs through fast holes transfer from ZnO@ZnS to CoS for surface water oxidation (Figs. S21 and S22).

To better understand the effect of visible light responsive MOF-derived ZnS/CoS on ZnO semiconductor performance,  $J$ - $V$  curves were also measured under visible light illumination ( $\lambda > 420 \text{ nm}$ ). The photocurrent densities of the ZnO@CoS and ZnO@ZnS/CoS photoanodes at 0.6 V were found to be  $1.21$  and  $1.08 \text{ mA cm}^{-2}$ , respectively (Fig. S23a). The largely enhanced photocurrent in response to visible light might be caused by the influence of the CoS decorating onto ZnO, where effectively visible light harvesting CoS could improve electron-holes separation. Then, the  $J$ - $V$  curves under chopped visible light illumination and corresponding photoconversion efficiency were further recorded for these photoanodes, further showing the improvement of photoconversion efficiency for ZnO@CoS and ZnO@ZnS/CoS (Figs. S23b and S24). Additionally,  $J$ - $V$  curves and EIS for all materials in the dark condition were recorded (Fig. S25). It was found that ZnO@ZnS/CoS and ZnO@CoS have good electrocatalytic activities, which can be attributed to such a fact that CoS acting as an efficient electrocatalyst

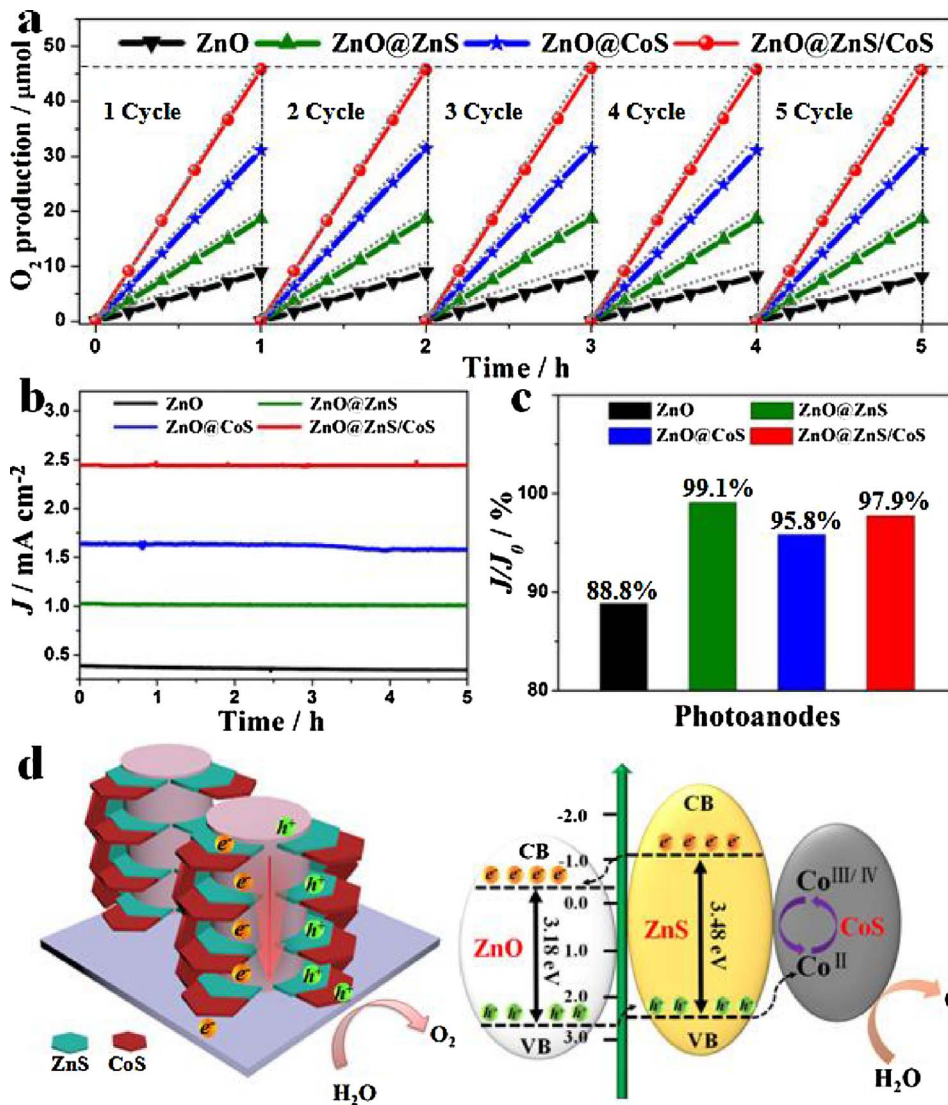


Fig. 5. (a) Amount of O<sub>2</sub> production measured by a gas chromatograph (the dashed lines are the calculated O<sub>2</sub> production from the photocurrent assuming 100% faradaic efficiency). (b) Chronoamperometry measurement and (c) retention of current density ( $J/J_0$ ) of ZnO, ZnO@ZnS, ZnO@CoS, and ZnO@ZnS/CoS at 0.6 V for 5 h under full spectrum illumination. (d) Schematic illustration of the PEC water oxidation process in the ZnO@ZnS/CoS system.

can promote the capture of holes and the reaction kinetics of water oxidation through the fast electron transfer between Co<sup>II</sup> and Co<sup>III</sup> [22,37], in accordance with the above results under visible light illumination (Fig. S25).

Furthermore, the oxygen production rates combined with photocurrents were monitored for testing the stability of four photoanodes. The ZnO@ZnS/CoS shows the largest average amount of O<sub>2</sub> production of 22.55 μmol h<sup>-1</sup> cm<sup>-2</sup> under full spectrum illumination, being 1.11, 2.32, and 4.69 times higher than that of ZnO@CoS, ZnO@ZnS, and ZnO, respectively, in accordance with the results under visible light illumination (Figs. 5 a and S26). And, the calculated faradaic efficiency by comparing with the actual O<sub>2</sub> production (Table S3) reveals that the sulfurization of MOFs onto ZnO greatly contributes to the stable PEC activity. Clearly, these MOF-derived ZnO-based photoanodes maintain high photocurrent densities under durative light illumination compared with the pristine ZnO (Fig. 5b). As shown in Fig. 5c, ZnO@ZnS/CoS, ZnO@CoS, ZnO@ZnS, and bare ZnO maintain 97.9, 95.8, 99.1, and 88.8% of photocurrent density after chronoamperometry measurement of five hours, respectively. The amount of O<sub>2</sub> production of bare ZnO shows a ~11% decline with decreasing faradaic efficiency to ~89% at the fifth cycle, resulting from the anodic photocorrosion. This was confirmed by the decreased weight ratio of O for ZnO after measurement (Fig. S27), probably because ZnO splits into O<sub>2</sub> [38,39]. On the contrary, the ZnO@ZnS/CoS, ZnO@CoS, and ZnO@ZnS show only 3, 6,

and 2% decay of initial photocurrent density after five cycles, respectively (Fig. 5c). And, the ZnO@ZnS/CoS maintained its microstructure and morphology after the measurements (Figs. S28 and S29). These results thus illustrate that the MOF-derivatives cellular structured shell could facilitate the efficient transfer of photo-induced electron/holes at the interface of photoanode/electrolyte and suppress the accumulation of holes, thereby avoiding the undesired photocorrosion/decomposition of the inner ZnO.

Based on above results, the mechanism for the enhanced photocurrent and photoconversion efficiency in the PEC water oxidation of ZnO@ZnS/CoS was proposed. As illustrated in Fig. 5d, firstly upon excitation by solar light, electrons are photoexcited from the valence band (VB) of ZnS to its conduction band (CB), followed by transferring to the highly-aligned ZnO nanorods, then fast migration via the inner structure to the current collector, and finally to the Pt counter electrode via the external circuit to be involved in formation of H<sub>2</sub>. On the other hand, the holes from the valence band (VB) of ZnS transfer to the VB of ZnO, resulting in a longer-lived hole in ZnS due to the efficient spatial separation of electron-hole pairs. Moreover, the photogenerated holes in ZnO/ZnS are fleetly transferred to the out surface to oxidize Co<sup>II</sup> to Co<sup>III</sup>/Co<sup>IV</sup> species in CoS. Subsequently, CoS employed as OEC can promote fast electron transfer and lower energy barrier of water oxidation, and simultaneously acted as a holes acceptor can facilitate the separation of photoexcited electrons-holes. In addition, the ZIF-derived

ZnS/CoS shell could contribute to the formation of surface passivation on the trap sites and defect states [40], and thus effectively suppress the accumulation of electron/holes through the synergistic effects from unique cellular structure and ternary heterojunction, which restrains the anodic decomposition/photocorrosion and thus improves the PEC stability.

#### 4. Conclusion

In summary, a feasible approach that the sulfurization of MOFs onto semiconductor ZnO to fabricate heterojunctions for PEC water oxidation is represented. The resulting ZnO@MOF-derivative photoanodes with cellular structure exhibit good PEC water oxidation performances. Particularly, the ZnO@ZnS/CoS represents a greatly enlarged photoconversion efficiency, photocurrent density, and low onset potential. It is proposed that the well-defined cellular structure of these composites with high surface area and unique porosity endows the efficient light utilization for reducing external energy consumption and rich exposed active sites for favorable reaction kinetics. The integration between inner ZnO and outer metal sulfides also affords suitable band matching for the efficient spatial separation of the photogenerated carriers and fast charge transfer. And, the catalyst CoS acting as OEC can promote the electron transfer on the surface of the heterojunction and improve the water oxidation kinetics. Simultaneously, visible light responsive CoS can act as a hole-trapping site and suppress the recombination of photogenerated electron-hole pairs. All these features contribute to the outstanding performance of ZnO@ZnS/CoS. This work thus provides a feasible and promising strategy to integrate the merits of novel MOF-derivative heterojunction with semiconductor into a novel photoanode system for the sustainable and affordable energy storage and conversion application.

#### Acknowledgements

This work was supported by the Natural Science Foundation of China (21576006 and 21606006); the China Postdoctoral Science Foundation (2016T90020); the Beijing Natural Science Foundation (2174064), and the Importation and Development of High-Caliber Talents Project of Beijing Municipal Institutions (CIT&TCD20150309).

#### Appendix A. Supplementary data

Supplementary data associated with this article can be found, in the online version, at <https://doi.org/10.1016/j.apcatb.2017.12.065>.

#### References

- [1] M.G. Walter, E.L. Warren, J.R. McKone, S.W. Boettcher, Q. Mi, E.A. Santori, N.S. Lewis, *Chem. Rev.* 111 (2010) 6446–6473.
- [2] C. Jiang, S.J.A. Moniz, A. Wang, T. Zhang, J. Tang, *Chem. Soc. Rev.* 46 (2017)

- 4645–4660.
- [3] D. Kim, K.K. Sakimoto, D. Hong, P. Yang, *Angew. Chem. Int. Ed.* 54 (2015) 3259–3266.
- [4] B. Zhang, Z. Wang, B. Huang, X. Zhang, X. Qin, H. Li, Y. Dai, Y. Li, *Chem. Mater.* 28 (2016) 6613–6620.
- [5] J.-W. Jang, C. Du, Y. Ye, Y. Lin, X. Yao, J. Thorne, E. Liu, G. McMahon, J. Zhu, A. Javey, J. Guo, D. Wang, *Nat. Commun.* 6 (2015) 7447.
- [6] O. Zandi, T.W. Hamann, *Nat. Chem.* 8 (2016) 778–783.
- [7] G. Liu, S. Ye, P. Yan, F. Xiong, P. Fu, Z. Wang, Z. Chen, J. Shi, C. Li, *Energy Environ. Sci.* 9 (2016) 1327–1334.
- [8] J. Han, Z. Liu, K. Guo, B. Wang, X. Zhang, T. Hong, *Appl. Catal. B Environ.* 163 (2015) 179–188.
- [9] Z. Wang, J. Han, Z. Li, M. Li, H. Wang, X. Zong, C. Li, *Adv. Energy Mater.* 6 (2016) 1600864.
- [10] H.M. Chen, C.K. Chen, Y.-C. Chang, C.-W. Tsai, R.-S. Liu, S.-F. Hu, W.-S. Chang, K.-H. Chen, *Angew. Chem. Int. Ed.* 49 (2010) 5966–5969.
- [11] Z. Wang, J. Hou, C. Yang, S. Jiao, K. Huang, H. Zhu, *Energy Environ. Sci.* 6 (2013) 2134–2144.
- [12] J. Li, S.K. Cushing, P. Zheng, T. Senty, F. Meng, A.D. Bristow, A. Manivannan, N. Wu, *J. Am. Chem. Soc.* 136 (2014) 8438–8449.
- [13] J. Du, J. Qi, D. Wang, Z. Tang, *Energy Environ. Sci.* 5 (2012) 6914–6918.
- [14] M. Wen, K. Mori, Y. Kuwahara, H. Yamashita, *ACS Energy Lett.* 2 (2017) 1–7.
- [15] D.K. Zhong, S. Choi, D.R. Gamelin, *J. Am. Chem. Soc.* 133 (2011) 18370–18377.
- [16] G. Ai, H. Li, S. Liu, R. Mo, J. Zhong, *Adv. Funct. Mater.* 25 (2015) 5706–5713.
- [17] T.W. Kim, K.-S. Choi, *Science* 343 (2014) 990–994.
- [18] M. Shao, F. Ning, M. Wei, D.G. Evans, X. Duan, *Adv. Funct. Mater.* 24 (2014) 580–586.
- [19] S.J.A. Moniz, S.A. Shevlin, D.J. Martin, Z.-X. Guo, J. Tang, *Energy Environ. Sci.* 8 (2015) 731–759.
- [20] S. Zhao, Y. Wang, J. Dong, C.-T. He, H. Yin, P. An, K. Zhao, X. Zhang, C. Gao, L. Zhang, J. Lv, J. Wang, J. Zhang, A.M. Khattak, N.A. Khan, Z. Wei, J. Zhang, S. Liu, H. Zhao, Z. Tang, *Nat. Energy* 1 (2016) 1–10.
- [21] M. Wen, K. Mori, T. Kamegawa, H. Yamashita, *Chem. Commun.* 50 (2014) 11645–11648.
- [22] F. Cao, M. Zhao, Y. Yu, B. Chen, Y. Huang, J. Yang, X. Cao, Q. Lu, X. Zhang, Z. Zhang, C. Tan, H. Zhang, *J. Am. Chem. Soc.* 138 (2016) 6924–6927.
- [23] J. Zhou, Y. Dou, A. Zhou, R.-M. Guo, M.-J. Zhao, J.-R. Li, *Adv. Energy Mater.* 7 (2017) 1602643.
- [24] M. Wen, K. Mori, Y. Kuwahara, T. An, H. Yamashita, *Appl. Catal. B Environ.* 218 (2017) 555–569.
- [25] P. He, X.-Y. Yu, X.W. Lou, *Angew. Chem. Int. Ed.* 56 (2017) 3897–3900.
- [26] M.-S. Yao, W.-X. Tang, G.-E. Wang, B. Nath, G. Xu, *Adv. Mater.* 28 (2016) 5229–5234.
- [27] W. Zhan, Y. He, J. Guo, L. Chen, X. Kong, H. Zhao, Q. Kuang, Z. Xie, L. Zheng, *Nanoscale* 8 (2016) 13181–13185.
- [28] W.-W. Zhan, Q. Kuang, J.-Z. Zhou, X.-J. Kong, Z.-X. Xie, L.-S. Zheng, *J. Am. Chem. Soc.* 135 (2013) 1926–1933.
- [29] Y. Dou, J. Zhou, A. Zhou, J.-R. Li, Z. Nie, *J. Mater. Chem. A* 5 (2017) 19491–19498.
- [30] Y.-N. Gong, T. Ouyang, C.-T. He, T.-B. Lu, *Chem. Sci.* 7 (2016) 1070–1075.
- [31] Y. Liu, Y. Gu, X. Yan, Z. Kang, S. Lu, Y. Sun, Y. Zhang, *Nano Res.* 8 (2015) 2891–2900.
- [32] R. Wu, D.-P. Wang, X. Rui, B. Liu, K. Zhou, A.W.K. Law, Q. Yan, J. Wei, Z. Chen, *Adv. Mater.* 27 (2015) 3038–3044.
- [33] L.-F. Shen, L. Yu, H.-B. Wu, X.-Y. Yu, X.-G. Zhang, *Nat. Commun.* 6 (2015) 6694.
- [34] L. Lin, T. Zhang, H. Liu, J. Qiu, X. Zhang, *Nanoscale* 7 (2015) 7615–7623.
- [35] J. Wang, S. Uma, K.J. Klabunde, *Appl. Catal. B Environ.* 48 (2004) 151–154.
- [36] F. Ning, M. Shao, S. Xu, Y. Fu, R. Zhang, M. Wei, D.G. Evans, X. Duan, *Energy Environ. Sci.* 9 (2016) 2633–2643.
- [37] C.-Y. Lin, D. Mersch, D.A. Jefferson, E. Reisner, *Chem. Sci.* 5 (2014) 4906–4913.
- [38] C.-H. Guo, J. Xie, H. Yang, C.-M. Li, *Adv. Sci. C* 2 (2015) 1500135.
- [39] J. Ishioka, K. Kogure, K. Oftuji, K. Kawaguchi, M. Jeem, T. Kato, T. Shibayama, S. Watanabe, *AIP Adv.* 7 (2017) 035220.
- [40] J. Han, Z. Liu, K. Guo, B. Wang, X. Zhang, T. Hong, *Appl. Catal. B Environ.* 163 (2015) 179–188.